

CORROSION BEHAVIOR OF HRB 400 REINFORCING STEEL WELDING JOINT IN SIMULATED CONCRETE ENVIRONMENT BASED ON SVET

KOROZIJSKO OBNAŠANJE ZVARNEGA SPOJA IZ OJAČANEGA JEKLA VRSTE HRB 400 V SIMULIRANEM OKOLJU IZ BETONA TEMELJEČEM NA TEHNOLOGIJI SVET

WenKai Zou¹, Chuanbo Zheng^{1*}, Han Ma², JiaQi He¹, XiaoBing Li¹,
JiMing Zhang², DianChun Ju¹, ChaoYang Zhou¹, Guo Yi¹

¹School of Metallurgical and Material Engineering, Jiangsu University of Science and Technology, Zhenjiang, 215600, Jiangsu, CHINA
²Jiangsu Shagang Group Co., Ltd. Shagang Research Institute, Zhenjiang, 257343, Jiangsu, China

Prejem rokopisa – received: 2023-12-07; sprejem za objavo – accepted for publication: 2024-04-08

doi:10.17222/mit.2024.1069

Based on SVET technology, the corrosion tendency of HRB400 steel welded joint and its base metal in simulated concrete environment and the influence of corrosion products were studied in this paper. The results show that the microstructure of the weld metal and base metal are ferrite+pearlite, and the microstructure of the heat affected zone is incompletely transformed bainite+ferrite+pearlite. Since the region produces smaller grains and more grain boundaries after welding, it becomes the most prone area for corrosion of welded joints. The addition of Cl^- inhibited the passivation of HRB400 steel welded joint in the simulated concrete pore fluid. Through the analysis of Nyquist curve and polarization curve, it was found that under high chloride ion concentration, the base metal is more sensitive to chloride ions compared to welded joints. With the increase of Cl^- concentration, the current density in the welded joint area gradually increased, but after reaching the chloride concentration of 0.5 mol/L, the current density tended to be flat. The occurrence of this phenomenon confirms the above conclusion. Further more, through SVET testing of the filler metal, it can be found that the filler metal has good adaptability to the HRB400 welding joint, forming a welding joint with better performance.

Keywords: corrosion of reinforced concrete, SVET, welded joints for reinforcing steel

Na osnovi tehnike vrstične vibrirajoče elektrode (SVET; angl.: Scanning Vibration Electrode Technique) so avtorji tega članka simulirali oziroma ugotavljali nagnjenost zvarnega spoja iz jekla vrste HRB400 h koroziji in njegove osnovne kovine v simuliranem okolju iz betona. V tem članku avtorji opisujejo vpliv nastalih korozijskih produktov. Rezultati preiskave kažejo, da imata kovina za varjenje in osnovni material feritno-perlitno mikrostrukturo in, da ima toplotno vplivana cona (HAZ; angl.: heat affected zone) nepopolnoma transformirano bainitno-feritno-perlitno mikrostrukturo. Ker je po varjenju področje zvara bolj drobno zrnato z več kristalnih mej, je jasno da je to tudi bolj nagnjeno h koroziji. Dodatek kloridnih ionov (Cl^-) ovira oziroma ustavi pasivacijo zvara iz jekla HRB400 v simuliranem okolju iz raztopine betona. Z analizo Nyquistove in polarizacijske krivulje so ugotovili, da visoka koncentracija kloridnih ionov bolj vpliva na osnovno kovino (izbrano jeklo) kot na varjeni spoj (zvar). Z naraščanjem koncentracije Cl^- ionov, gostota električnega toka v zvaru postopoma narašča, toda nad koncentracijo kloridnih ionov 0,5 mol/L ostaja le-ta konstantna. Pojav tega fenomena potrjujejo zgoraj navedeni zaključki. Nadalje so avtorji s pomočjo tehnologije SVET testirali material za varjenje in ugotovili, da se dobro ujema z zvarom iz jekla HRB400 in pri tem tvori zvarni spoj z boljšimi lastnostmi.

Ključne besede: korozija ojačanega betona, tehnika vrstične vibrirajoče elektrode, zvarni spoji za ojačano jeklo

1 INTRODUCTION

Reinforced concrete is currently widely used in various construction fields around the world.¹ Generally, Reinforced concrete has high durability and can withstand different harsh working environments.² The high-alkalinity concrete pore liquid will provide strong protection for the rebars, keep the rebars in a passivated state, and effectively avoid corrosion of the rebars.³ However, in the actual construction process, factors such as improper design, lax construction, and the intrusion of corrosive ions in the environment often accelerate the corrosion of rebars,⁴ causing significant loss of steel bar sections,

which in turn leads to the destruction of reinforced concrete structures. As the most important form of damage to reinforced concrete structures,⁶ the various direct and indirect safety and economic losses caused by steel corrosion cannot be ignored.⁷ According to a special research conducted by the Committee on Transportation Research of the United States National Research Council,⁸ the annual economic damages incurred by concrete bridges in the United States due to the utilization of de-icing salt range from \$0.35 billion to \$1 billion.⁹ It can be seen that studying the corrosion behavior of rebars in concrete is of great significance to the construction field.

The scanning vibration electrode technique (SVET) used in this article is an electrochemical testing method

*Corresponding author's e-mail:
zhengchuanbo@just.edu.cn (Chuanbo Zheng)

Table 1: Main chemical composition of HRB400 and welding wire

Materials	C	Si	Mn	P	S	Protective gas
HRB400	0.2302	0.4351	1.4324	0.0135	0.0177	
Welding wire	0.10	0.64	1.26	0.011	0.012	80%Ar-20%CO ₂

that has several significant advantages and innovations compared to traditional electrochemical techniques:

High sensitivity and spatial resolution: SVET can achieve real-time monitoring of electrochemical reactions at the microscopic scale, with spatial resolution reaching sub micron level. According to literature review,¹⁰ the spatial resolution of general electrochemical testing can only reach the millimeter level. This high sensitivity and spatial resolution give SVET unique advantages in studying micro electrochemical processes, corrosion behavior, and corrosion protection materials.

Non destructive: SVET technology does not require destructive operations on the tested sample, as it only involves scanning a tiny probe on the surface of the sample.¹¹ This makes SVET an ideal tool for studying material corrosion, anti-corrosion coating performance, and other aspects

Real time performance: SVET can monitor electrochemical processes in real time,¹² providing real-time information about reaction kinetics and process dynamics, which is crucial for a deeper understanding of electrochemical reaction mechanisms.

Multifunctionality: SVET technology can be combined with other technologies,¹³ such as scanning electron microscopy (SEM), to achieve multi angle and multi-scale characterization of electrochemical processes, providing the possibility for deeper research.

The innovation of SVET technology mainly lies in its application to vibration probes. Traditional electrochemical testing methods often use static probes,^{14–17} while SVET utilizes the characteristics of vibration probes to achieve high sensitivity electrochemical testing through the electrochemical interaction between the vibration probe and the electrolyte solution.¹⁸ In addition, the development of SVET also benefits from the advancement of micro nano technology, making the preparation and operation of SVET systems more convenient and accurate.¹⁹

At present, the general corrosion tendency of HRB400 reinforced concrete has been clarified, but there is little research on the corrosion behavior of its welded joints in concrete systems, and there is little research using SVET methods. Therefore, this study aims to study the corrosion tendency and reasons of HRB400 steel welded joints in concrete systems using SVET method, in order to provide further process optimization ideas for construction engineering and materials fields, and to promote the further development of reinforced concrete anti-corrosion engineering.

2 EXPERIMENTAL PART

2.1 Preparation of the welded joint

The welding materials utilized comprise HRB400 threaded steel and MG-51T low-carbon solid welding wire, with their compositions as illustrated in **Table 1**.

The welding experiments were conducted using a Metal Inert Gas (MIG) composite welding method, employing a flat butt joint configuration.²⁰ The welding wire used was a low-carbon solid welding wire, and a 0.5 mm gap was maintained during assembly to ensure the alignment of the two plates as closely as possible. Throughout the entire welding process, both the front and back sides of the weld were shielded with pure Ar gas. The gas flow rate at the front was set at 30 L/min, while at the back, it was 5 L/min. The welding parameters were as follows: welding current ranging from 130–150 A, welding voltage from 23–25 V, and welding speed at 0.667 cm/s.

2.2 Corrosion system simulation

This paper uses the method of simulating concrete pore fluid to study the corrosion process of HRB400 reinforcement welded joints and the effect of adding different concentrations of NaCl on joint corrosion. Take the saturated Ca(OH)₂ supernatant with a pH value of 12.5 as the simulated concrete pore liquid, and add NaCl to obtain a chlorine-containing salt simulated concrete pore liquid.

Following this, Cut out the parts of the HRB400 reinforcement welded joint that need to be tested and encapsulate them with denture-based resin; connect copper wires behind them. After encapsulation, polish the test surface with 240#, 400#, 600#, 800#, 1000#, 1500# and 2000# sandpaper in sequence until the surface is bright. After polishing, use alcohol to remove surface stains, rinse with distilled water, and blow dry. use. In the experiment, P.O 42.5 ordinary Portland cement and limestone mineral powder were used as composite cementitious materials, and carbon nanotubes and PAN-based carbon fibers were used as conductive fillers. The composition and proportion of conductive concrete are shown in **Table 2**. (Conductive fillers will only play a role in electrochemical testing.) The working surface of the specimen was then evenly covered with a layer of concrete with a thickness of 0.5 cm. Conduct electrochemical tests after one day of curing. The encapsulated samples were placed in a saturated Ca(OH)₂ solution with a concentration of 0.5 mol/L NaCl for one day and then electrochemical tests were performed,²⁰ The working electrode is shown in **Figure 1**.

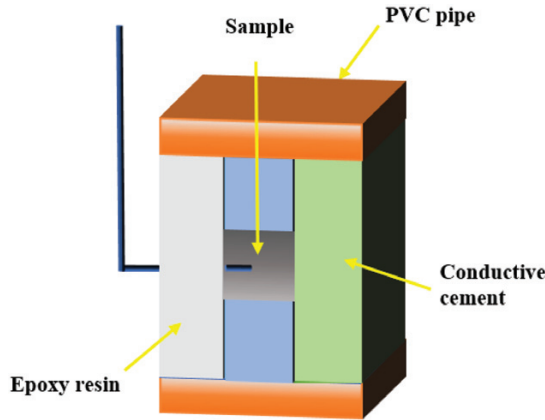


Figure 1: Schematic diagram of working electrode

2.3 Electrochemical testing

The electrochemical workstation utilized for the macroscopic electrochemical testing was the Donghua electrochemical workstation. For macroscopic electrochemical measurements, a corrosion cell with three electrodes was utilized. The working electrode was the reinforcement welded joint, the counter electrode was a platinum sheet electrode, and the reference electrode was a mercury oxide electrode. Following the attainment of a stable open-circuit potential (OCP), a series of electrochemical impedance spectroscopy (EIS) and potentiodynamic polarization curve experiments were conducted in a sequential manner. In the context of Electrochemical Impedance Spectroscopy (EIS), the frequency range utilized for impedance testing spanned from 10^5 Hz to 10 mHz. This range was subjected to a sine wave excitation signal with an amplitude of 10 mV. During the process of conducting polarization curve measurements, the beginning potential relative to the open circuit potential (OCP) was established at -0.8 V (HgO), whereas the final po-

tential relative to the OCP was set at 1.2 V (HgO). EIS data obtained by equivalent circuit fitting based on ZSimpWin software. Microelectrochemical tests were performed using a Princeton VersaSCAN microscopy scanning electrochemical workstation (AMETEK Inc., California, USA). The surface vibrational spectroscopy and electrochemical technique (SVET) method is used to quantify the difference in potential within the solution, thereby indicating the local current present on the sample surface, and reflecting the inhomogeneity of the electrochemical activity on the sample surface through three-dimensional images. To ensure accuracy, multiple measurements were taken for each test, repeated at least three times (include SVET tests). The presented results are representative of the selected ones. In addition, the test temperature is always maintained at 20 °C.

3 RESULTS

3.1 Microstructure analysis

Microstructural analysis explains the corrosion susceptibility of the welded joint. This is attributed to local differences in the microstructure, such as grain size and elemental composition, which can result in varying corrosion performance. Figure 2 depicts microstructural images of the reinforcement welded joint, where the weld metal and base material is primarily composed of ferrite and pearlite, while the heat-affected zone comprises partially untransformed bainite, quasi-polygonal ferrite, acicular ferrite, and pearlite. The microstructure of the heat-affected zone indicates that its surface is more active, with smaller grains and more grain boundaries, both of which make it more susceptible to corrosion.²¹⁻²⁴ Moreover, when taking into account the phase composition, The coexistence of ferrite and bainite phases in the heat affected zone is expected to lead to more corrosion than in other parts of the welded joint (ferrite + pearlite).

Table 2: Conductive concrete ratio

Raw material consumption (kg/m ³)				Carbon nanotubes /%	PAN-based carbon fiber /%	Water reducing agent /%	Defoamer /%
Cement	Coal ash	Mineral powder	Water				
280	33.6	50.4	140	0.2	0.3	1	0.1

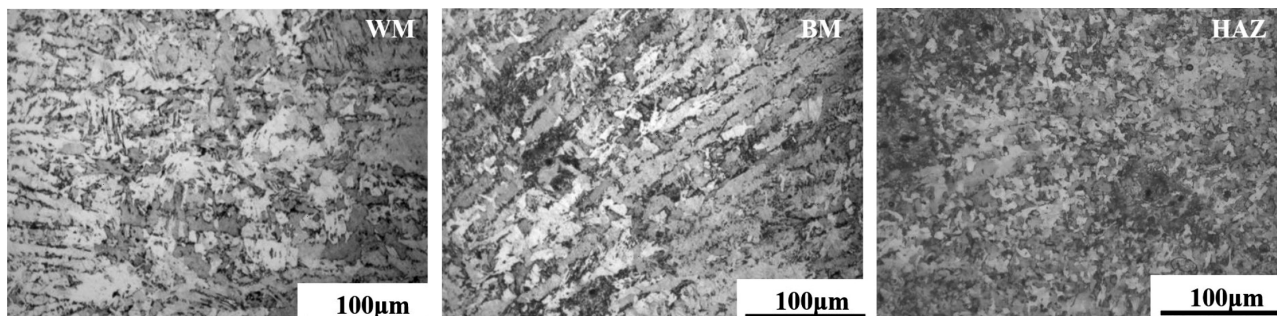


Figure 2: Microstructural Morphology of the Welded Joint

3.2 Local corrosion behavior in different parts of joint

Figure 3 shows the polarization curves of welded joints, and base metal under simulated concrete pore solution of 0.5 mol/L NaCl. The graphic illustrates that both the welded joint and the base metal undergo three separate zones, namely the activation region, the passivation region, and the overpassivation region. In the activation zone, there is a rapid occurrence of the development of surface passivation film products, and the reactions on the metal surface proceed at a high rate. Once the passivation region is reached, corrosion becomes stable within this specific range of potential, resulting in smaller fluctuations in current values. The main factor contributing to this phenomenon is principally associated with the significantly alkaline properties of the simulated concrete pore solution, which effectively stabilizes the existence of calcium aluminate chloride. The presence of corrosive anions, such as chloride ions (Cl⁻), is effectively impeded by the passivation film at defects in the welded joint.²⁵ In the region of overpassivation, when the potential reaches a specific threshold, the passivation film on the metal surface is compromised, leading to pitting corrosion and a substantial escalation in the corrosion rate.²⁶ The passivation range of the welded joint has a noticeably smaller scope in comparison to that of the base material. Indicating that it is difficult to form a complete passivation film on welded joints under simulated pore fluid conditions.²⁷ In addition, it is observed that the self-corrosion potential of the welded joint is comparatively lower, suggesting a significantly diminished level of corrosion resistance in comparison to the base material.²⁷ Detailed corrosion parameters are shown in Table 3. According to previous research,²⁸ the partial microstructure contained in welded joint is more likely to become the area where corrosion begins. In order to visually understand the corrosion resistance performance of each area of the welded joint, the joint is divided into

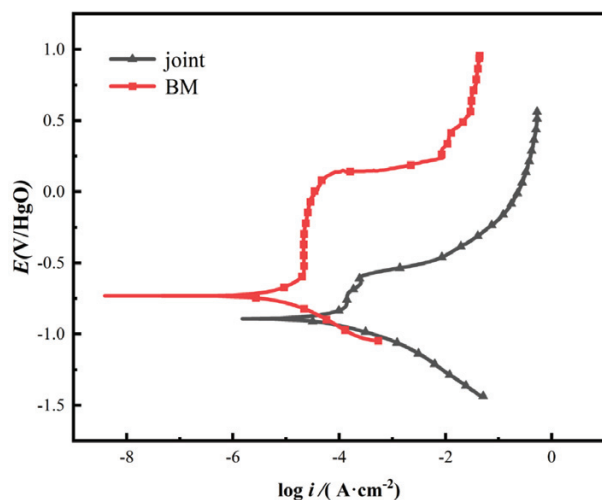


Figure 3: Polarization curves of joint and base metal under 0.5 mol/L NaCl saturated

weld metal (i.e. fusion zone), base metal, and heat affected zone for SVET testing.

Table 3 Corrosion parameters of welded joints and base material

Specimens	$i_{corr} / A \text{ cm}^{-2}$	E_{corr} / V
Joint	7.02×10^{-5}	-0.869
BM	1.45×10^{-5}	-0.795

The results of the SVET (Surface Vibrational Spectroscopy and Electrochemical Technology) test for different locations of the welded joint under 0.5 mol/L sim-

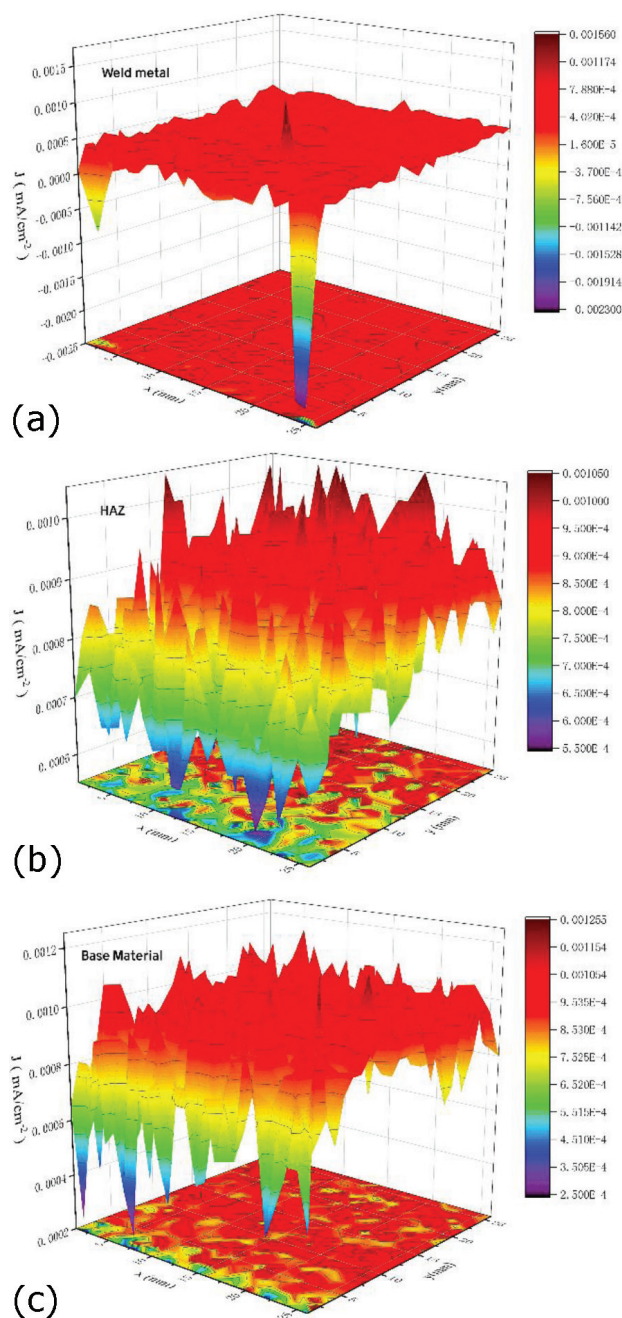


Figure 4: SVET images of welded joints immersed in 0.5 mol/L NaCl simulated concrete pore solution for 24 h

ulated concrete pore liquid are depicted in **Figure 4**. The examination utilizes a blend of three-dimensional representations and two-dimensional planar images for the purpose of visualization. The three-dimensional representations provide a comprehensive depiction of the variations in current density over the surface of sample. The use of Scanning Vibrating Electrode Technique (SVET) enables the deduction of corrosion activity at regions where defects are present by continuous scanning. The fluctuations observed in the data are indicative of micro anode and microcathode currents, with the peaks representing the former and the troughs representing the latter.²⁹ The chosen micro-area three-dimensional map displays a prominent anode peak, indicating that the current fluctuations around the anode peak are large. These areas are likely to be the areas where corrosion occurs around the sample,³⁰ dissolution occurs earlier in the corrosive solution, destroying the passivation film on the joint surface, causing the substrate to be exposed in the solution, becoming the anodic phase and starting to activate corrosion. It can be found that the fluctuations in the three-dimensional diagram of the weld metal are relatively gentle, and the difference in current density values is small, indicating that the anode current changes slowly in this area, the probability of surrounding corrosion is low, and the sample surface still has a good layer of protection in the solution to inhibit the occurrence of corrosion. Simultaneously, in the three-dimensional image of the heat-affected zone, it can be clearly seen that the anode peak is lower away from the weld area, and the anode peak gradually becomes larger after approaching the weld area. The complete three-dimensional image exhibits a fluctuating and irregular pattern, whereas the anode current displays a significant disparity. This is because the local area near the fusion line has higher thermal stress and is more prone to corrosion.³¹ Upon comparing the SVET images of the three distinct portions, it becomes apparent that the weld metal region exhibits a lower susceptibility to corrosion in comparison to both the base material and the heat-affected zone. In contrast, it can be shown that the heat-affected zone exhibits the highest susceptibility to corrosion start, a finding that is consistent with the outcomes derived from the polarization tests. In order to accurately evaluate the corrosion behavior of each part of the welded joint using SVET data,³² the data in **Table 4** are calculated using the following formulas:

$$I_c = \int_0^{X_{max}} \int_0^{Y_{max}} [j_z(x, y) < 0] dx dy \quad (1)$$

$$I_a = \int_0^{X_{max}} \int_0^{Y_{max}} [j_z(x, y) > 0] dx dy \quad (2)$$

$$I = \frac{|I_a| + |I_c|}{2} \quad (3)$$

Table 4: SVET data in 0.5 mol/L NaCl saturated Ca (OH)₂ solution in each region of the welded joint

Specimens	$J / (\text{mA} \cdot \text{cm}^{-2})$
HAZ	1.25
Weld metal	0.442
BM	0.881

3.3 Corrosion products

Before studying the micro effects of chlorides on welded joints, it is best to first understand what corrosion products are present in the welded joints in this concrete system, in order to conduct a reasonable analysis of subsequent experimental results. Therefore, XRD experiments were conducted, and the results are as follows: The X-ray diffraction (XRD) spectra of the welded joint following a 10-day corrosion period in a 0.5 mol/L sodium chloride (NaCl) Simulated concrete pore fluid is depicted in **Figure 5**. **Figure 5** illustrates that the constituents present on the surface of the welded joint predominantly consist of CaCO₃, Fe₂O₃, and CaCl₂. Fe₂O₃ is a corrosion product in this system.³³ The presence of Fe₂O₃ suggests that corrosion has taken place on the surface of the welded joint.

3.4 Impact of chloride ion concentration on local corrosion resistance

EIS experiment and Tafel polarization curve are the most common experiments reflecting corrosion tendency. Before the subsequent test, the EIS test and Tafel polarization can be used for macro and local comparison. The EIS fitting data are shown in **Tables 5** and **6**. In the equivalent circuit, R_s is the solution resistance, R_f is the passivation film resistance, Q_1 is the common phase angle element, which includes the passivation film capacitance C_f and the dispersion coefficient n_1 , R_{dl} is the charge transfer resistance, Q_2 is the common phase angle

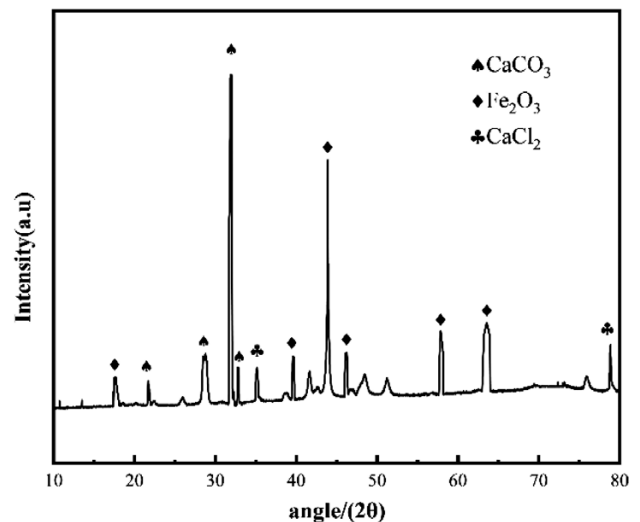


Figure 5: XRD Spectrum of the Welded Joint Surface After 10 Days of Corrosion

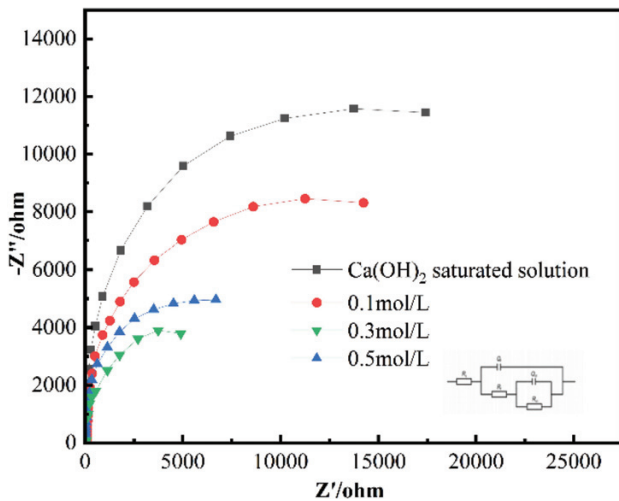


Figure 6: Impedance Spectrum of Welded Joints in Simulated Concrete Pore Solutions with Various Chloride Ion Concentrations

element, These include the electric double layer capacitance C_{dl} and the dispersion coefficient n_2 . The value of the diffusion coefficient n is usually between 0 and 1.³⁴ Research shows that the value of n is related to the uniformity and compactness of the surface passivation film.³⁵ The smaller the value of n , the more grain boundaries, defects, and impurities exist on the surface of the material. The worse the uniformity and density of the passivation film.³⁶ In the circuit, Q_1 simulates the complete area of the passivation film, and Q_2 simulates the double electric layer at the rupture point of the passivation film or the defect potential.³⁷ From **Figure 6**, it can be seen that as the concentration of chloride ions increases, the performance of the passive film formed by the joint gradually decreases. However, the performance of the passive film formed by the joint at 0.5 mol/L is higher than that at 0.3 mol/L. According to the Nyquist curve of the base material in **Figure 7**, the passivation film performance of the base material rapidly decreases with the increase of chloride ion concentration. When reaching a high concentration, the capacitance arc of the

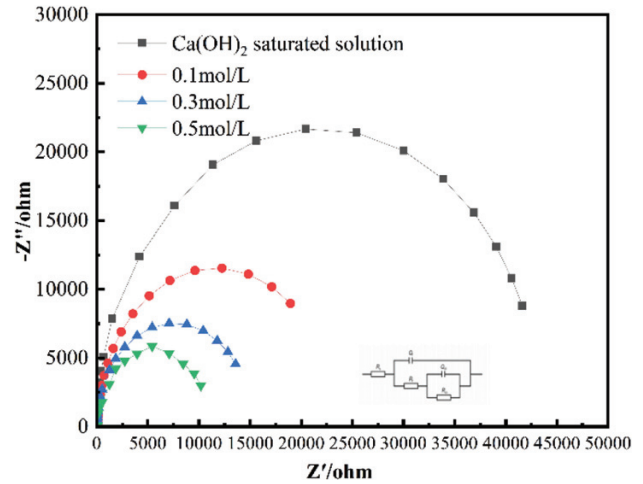


Figure 7: Impedance Spectrum of Base Material in Simulated Concrete Pore Solutions with Different Chloride Ion Concentrations

base material curve is already close to that of the joint curve. This indicates that at high chloride ion concentrations, the performance of the passivation film formed on the surface of the base material and the joint is relatively close.

According to the polarization curves shown in **Figures 8 and 9**, it can be observed that at low chloride ion concentrations, corrosion of the joint and substrate materials does not occur significantly, and there is a phenomenon of secondary passivation in both the base material and the joint, and it can be observed that there is a noticeable decline in the corrosion resistance of the welded joint as the concentration of Cl^- increases. The observed phenomenon can be attributed to the build-up of chloride ions (Cl^-) at the sites of defects during the passivation process of the metal.²⁵ This buildup leads to the formation of localized activation spots and consequently accelerates the pace at which the material dissolves.²⁸ An increase in the concentration of chloride ions (Cl^-) results in a corresponding increase in their adsorption onto the substrate's surface.³⁸ Consequently, this heightened adsorption contributes to the exacerbation of corrosion.³⁹

Table 5: EIS fitting parameters for corrosion of welded joints in simulated concrete pore fluids with different chloride ion concentrations

Cl^- concentration /mol·L ⁻¹	$R_s / \Omega \cdot cm^2$	$R_f / \Omega \cdot cm^2$	$Q_f / \Omega^{-1} \cdot cm^{-2} \cdot s^{-1}$	n_f	$R_{ct} / \Omega \cdot cm^2$	$Q_{dl} / \Omega^{-1} \cdot cm^{-2} \cdot s^{-1}$	n_{dl}
0	3.04	2.18×10^4	1.34×10^{-5}	0.86	1.77×10^4	3.84×10^{-5}	0.68
0.1	3.12	2.47×10^4	5.82×10^{-5}	0.88	1.59×10^4	2.26×10^{-4}	0.71
0.3	4.76	4.98×10^4	8.13×10^{-5}	0.93	1.89×10^4	4.17×10^{-4}	0.79
0.5	3.98	4.16×10^4	6.82×10^{-5}	0.91	1.72×10^4	3.43×10^{-4}	0.74

Table 6: EIS fitting parameters of base metal corrosion in simulated concrete pore fluids with different chloride ion concentrations

Cl^- concentration /mol·L ⁻¹	$R_s / \Omega \cdot cm^2$	$R_f / \Omega \cdot cm^2$	$Q_f / \Omega^{-1} \cdot cm^{-2} \cdot s^{-1}$	n_f	$R_{ct} / \Omega \cdot cm^2$	$Q_{dl} / \Omega^{-1} \cdot cm^{-2} \cdot s^{-1}$	n_{dl}
0	3.01	1.82×10^4	1.05×10^{-5}	0.85	1.82×10^4	4.01×10^{-5}	0.66
0.1	3.09	2.15×10^4	5.74×10^{-5}	0.88	1.56×10^4	2.19×10^{-4}	0.57
0.3	3.55	3.68×10^4	6.79×10^{-5}	0.78	1.66×10^4	3.15×10^{-4}	0.67
0.5	3.97	4.17×10^4	7.83×10^{-5}	0.91	1.84×10^4	3.96×10^{-4}	0.77

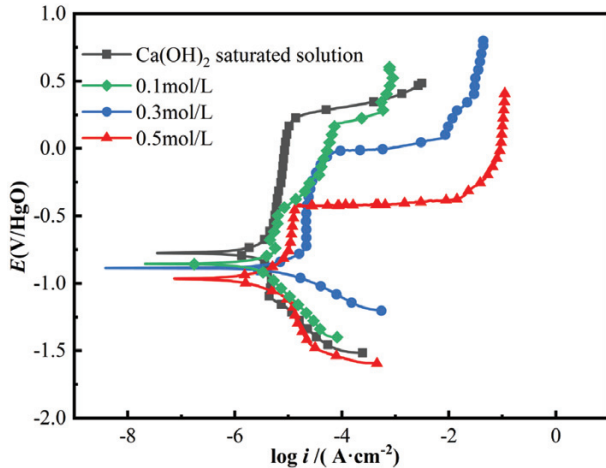


Figure 8: Polarization curves of the base material in simulated concrete pore solutions with different chloride ion concentrations

According to the values in Table 7, in a solution containing NaCl at an equivalent concentration, it is seen that the self-corrosion current density of the welded joint surpasses that of the base material. This difference means that the base material exhibits greater corrosion resistance. By comparing the absolute difference in i_{corr} between the welded joint and the base metal at high concentrations (0.3–0.5 mol/L), it can be found that the absolute difference in i_{corr} between the welded joint and the base metal is 1.75×10^{-5} , and the absolute difference in i_{corr} between the base metal and the base metal is 1.771×10^{-5} . It can be seen that the sensitivity of the base metal to chloride ion concentration is higher than that of the welded joint at high concentrations. It is worth noting that when the chloride ion concentration reaches 0.5 mol/L, the self corrosion current density of welded joints decreases compared with 0.3 mol/L. A similar situation occurred in the EIS test, which is not consistent with the general rule of previous studies.³⁴ Although a large number of repeated tests have been carried out, the possibility of contingency cannot be

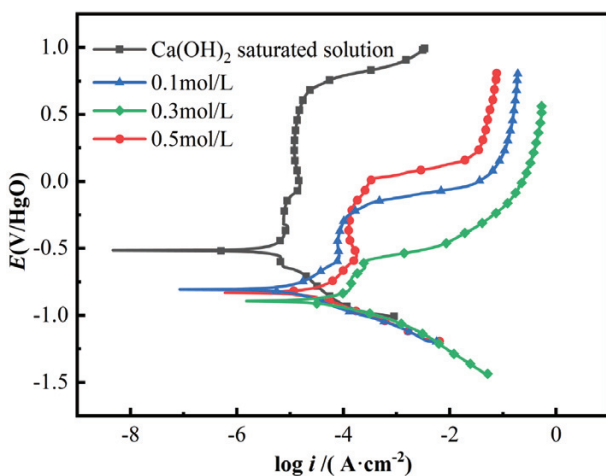


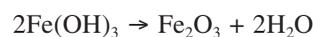
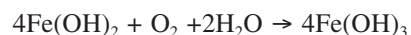
Figure 9: Polarization curves of the welded joint in simulated concrete pore solutions with different chloride ion concentrations

ruled out. Therefore, Further detailed testing was conducted on the corrosion trend in local areas of welded joints using SVET technology.

Table 7: Corrosion parameters of base metal joints under different chloride ion concentrations

Sample	Cl ⁻ concentration/mol·L ⁻¹	i_{corr} /A·cm ²	E_{corr} / V
BM	0	4.06×10^{-6}	-0.784
	0.1	4.23×10^{-6}	-0.796
	0.3	4.79×10^{-6}	-0.813
	0.5	2.25×10^{-5}	-0.824
Joint	0	3.56×10^{-6}	-0.506
	0.1	1.08×10^{-5}	-0.817
	0.3	4.17×10^{-5}	-0.884
	0.5	2.42×10^{-5}	-0.828

Figure 10 shows the evolution of current density distribution of welded joints after soaking in simulated concrete pore solution of (0, 0.1, 0.3 and 0.5) mol/L NaCl for 1 h respectively. It can be found that in four different solutions, at the beginning of the corrosion stage, the current density at the microlocation was not unified and showed peaks and valleys, indicating that anodic and cathodic localized corrosion occurred. When the concentration of chloride ion is 0 mol/L, the local current is generally flat without too much fluctuation, This is because under normal alkaline environment, the passivation film on the surface of welded joints has high integrity, and pitting corrosion will hardly occur.⁴⁰ With the chloride ion concentration continuously increasing to 0.3 mol/L, the average current density of each region of the welded joint generally increased, and the anode peak appeared in some regions.⁴¹ When the current increases and the current position increases, it can be confirmed that pitting corrosion has occurred on the surface of the welded joint.¹⁹ And the pitting sites were more evenly distributed and numerous,⁴² with a large cathode and a small anode.⁴³ This is related to the grain size changes and possible residual stresses in the welded joints mentioned earlier. During the corrosion process, residual stress easily causes chloride ions to migrate along the stress gradient, making it easy for pitting corrosion to occur in the welded joint. However, when the concentration of chloride ion reaches 0.5 mol/L, the current density in the micro zone of the welded joint has a downward trend.⁴⁴ According to the XRD test results, it is not difficult to infer that there are corrosion products in the joint after 1 h immersion, namely:



At the same time, high concentration of OH⁻ can effectively inhibit the accumulation of Cl⁻ in the passive film defects,³⁶ therefore, when the concentration rises to 0.5 mol/L, the current density in the micro region will

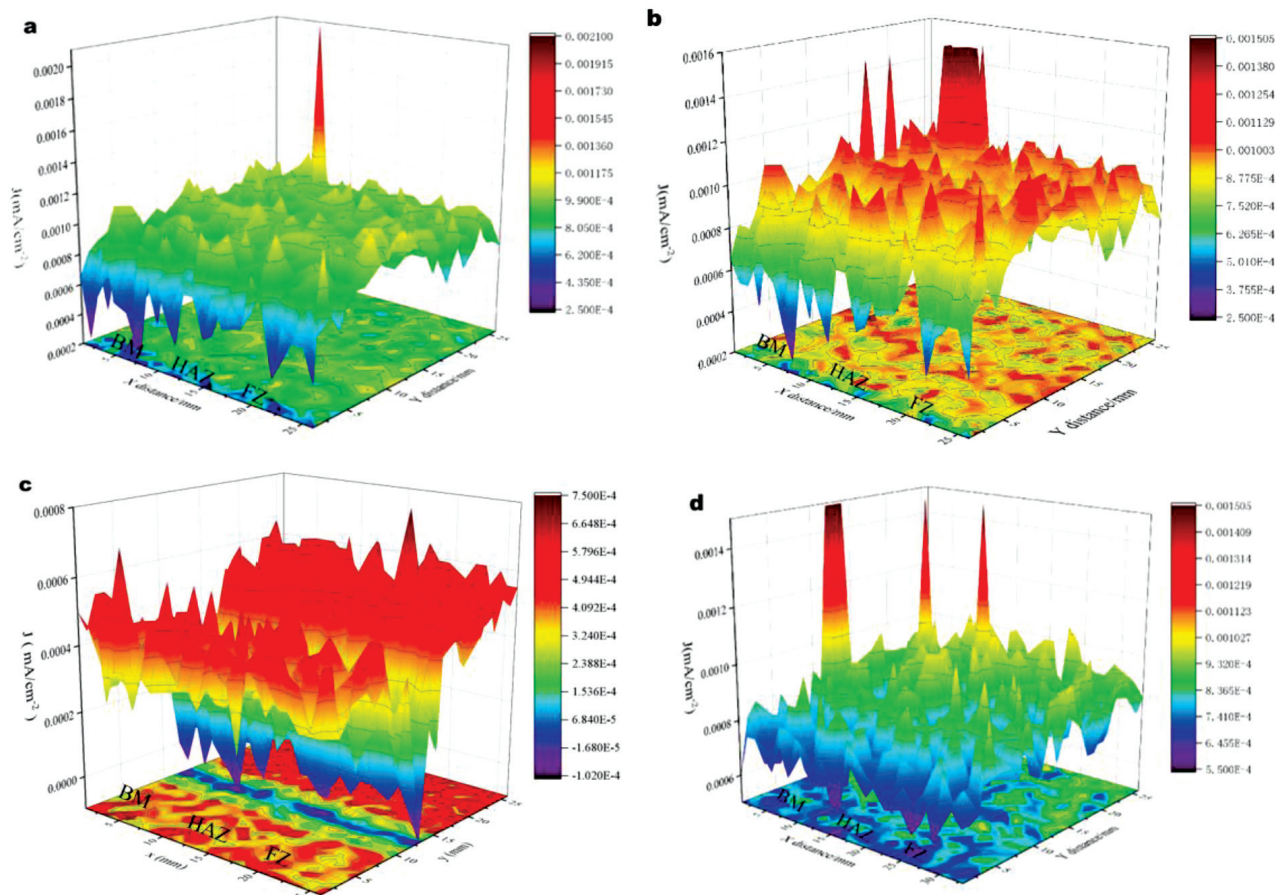


Figure 10: Current density distribution of welded joints after immersion for 24 h under different chloride ion concentrations: a) 0 mol/L, b) 0.1 mol/L, c) 0.3 mol/L, d) 0.5 mol/L

tend to be flat.⁴⁵ This is also consistent with the polarization curve and EIS results.

4 DISCUSSION

Based on the research by Nedal,³ it is not difficult to find the general conclusion that as the concentration of chloride ions invading the concrete system increases, the corrosion rate of the entire reinforced concrete system will increase. In this study, the results of the Nyquist curve and polarization curve confirmed that the HRB400 steel bar welding joint will generate a better passivation film than the base metal under high chloride ion concentration. That is to say, at high chloride ion concentration (0.5 mol/L), the HRB400 steel bar welding joint will show better corrosion resistance. After further SVET testing, this conclusion was also confirmed. Meanwhile, through the comparison of SVET testing results, it was found that the HRB400 steel bar welding joint made by previous researchers showed higher anode current density in the fusion line area,¹⁰ followed by HAZ. According to the SVET test results in this article, the anode current density at the HAZ of the welded joint is much higher than that in other areas, which means that the filler weld metal used in this article has better phase with

the HRB400 steel reinforcement welded joint, making it a higher quality welded joint in concrete environments.

5 CONCLUSIONS

(1) Observation results based on micro-appearance, in HRB400 welded joints, The microstructure of the weld metal and base metal is a ferrite+pearlite, and the structure of the heat-influencing area is bainite that are not fully transformed+ferrite+pearlite. Combined with the results of SVET test, it can be confirmed that this area in the welded joint is most prone to corrosion, because smaller grains and more grain boundaries are formed, the probability of defects occurring is the highest.

(2) According to the results of the SVET test, the anode corrosion current density in the heat affected zone of HRB400 steel welded joint is the highest, reaching 1.25 mA·cm⁻². The closer to the HAZ, the faster the anode current changes, and the more prone to corrosion. Based on other electrochemical test fitting data results, compared to welded joints, the base metal has a higher sensitivity to chloride ion viscosity at high concentrations, and the performance of the passivation film formed between the base metal and the joint tends to be consistent at high concentrations. Moreover, based on the

SVET test results of the weld metal, the corrosion resistance of the filled area is relatively excellent, and it has good compatibility with the joint.

(3) SVET and XRD results show that when the chloride ion concentration increases, the local current density distribution on the welded joint surface changes from uniform to uneven, but when it reaches 0.5 mol/L, the local current density tends to be flat again. On the basis of analyzing the formation process of corrosion products in this experiment, considering that the OH⁻ and Cl⁻ in the corrosion products are adsorbed and competed on the surface of the welded joint, which makes the welded joint more resistant to Cl⁻ with a higher concentration (0.5 mol/L).

6 REFERENCES

- ¹ W. Hou, Y. Ding, G. Huang, N. Huda, L.H.A. Shah, Z. Piao, Y. Shen, Z. Shen, A. Gerlich, The role of pin eccentricity in friction stir welding of Al-Mg-Si alloy sheets: microstructural evolution and mechanical properties, *The International Journal of Advanced Manufacturing Technology*, (2022). doi:10.1007/s00170-022-09793-x
- ² Z. Li, S. Lv, Database on Corrosion of Ocean Engineering Materials and Structures, in: *Proceedings of the 2(nd) Asian Materials Database Symposium*, 2010
- ³ M. Nedal, M. Boulfiza, R. Evitts, Corrosion of Carbon Steel and Corrosion-Resistant Rebars in Concrete Structures Under Chloride Ion Attack, *Journal of Materials Engineering & Performance*, (2013)
- ⁴ Z. Li, Anti-corrosion measures of concrete bridge structure durability under ocean environment, *Shanxi Architecture*, (2012)
- ⁵ R. J. Himiob, Evaluation of corrosion resistant ferrous-alloys in chloride contaminated concrete, in, *Florida Atlantic University*, 2007
- ⁶ R. E. Melchers, I. A. Chaves, A comparative study of chlorides and longer-term reinforcement corrosion, *Materials and Corrosion*, 68 (2017). doi:10.1002/maco.201609310
- ⁷ S. G. Dong, B. Zhao, C. Lin, R. G. Du, R. G. Hu, G. X. Zhang, Corrosion behavior of epoxy/zinc duplex coated rebar embedded in concrete in ocean environment, *Construction & Building Materials*, 28 (2012), 72–78
- ⁸ B. Qiao, D. U. Ronggui, W. Chen, Y. Zhu, C. Lin, Effect of NO²⁻ and Cl⁻ on the corrosion behavior of reinforcing steel in simulated concrete pore solutions, *Acta Metallurgica Sinica -Chinese Edition*, (2010) 245–250. doi:10.3724/SP.J.1037.2009.00376
- ⁹ Y. Zhao, J. Yu, W. Jin, Damage analysis and cracking model of reinforced concrete structures with rebar corrosion, *Corrosion science*, 53 (2011) 3388–3397. doi:10.1016/j.corsci.2011.06.018
- ¹⁰ S. Yan, H. Chen, C. Ma, Y. Nie, X. Wang, Q. H. Qin, Local corrosion behaviour of hybrid laser-MIG welded Al-Zn-Mg alloy joints, *Materials & Design*, 88 (2015) 1353–1365. doi:10.1007/978-3-642-45232-1_61
- ¹¹ S. Coccia, S. Imperatore, Z. Rinaldi, Influence of corrosion on the bond strength of steel rebars in concrete, (2014). doi:10.1617/s11527-014-0518-x
- ¹² Y. B. Yang, S. Liang, H. H. Mo, Y. W. Chen, The Experimental Study of Anti-seawater Corrosion Concrete with a Lot of Slag at Ocean Environment, *Journal of Wuhan University of Technology*, (2005)
- ¹³ C. Qi, G. Guisheng, L. Feng, W. U. Sanyu, Z. Dalin, A New Type Anticorrosion Coating for Ocean Reinforced Concrete Structures, *China Ocean Engineering (English version)*, 014 (2000) 385–390. doi:10.3321/j.issn:0890-5487.2000.03.013
- ¹⁴ T. Morita, M. Yamanaka, Microstructural evolution and mechanical properties of friction-stir-welded Al-Mg-Si joint, *Materials Science & Engineering A*, 595 (2014) 196–204
- ¹⁵ Cai, J., Ma, H., Zhou, Y., Chen, C., Liu, Corrosion behaviour of low alloy corrosion resistant steel in simulated concrete environment, *Materials Research Innovations*, (2014)
- ¹⁶ W. K. Green, Steel reinforcement corrosion in concrete – an overview of some fundamentals, *Corrosion Engineering Science and Technology*, 55 (2020), 1–14. doi:10.1080/1478422X.2020.1746039
- ¹⁷ S. Yan, Y. Nie, Z. Zhu, H. Chen, G. Gou, J. Yu, G. Wang, Characteristics of microstructure and fatigue resistance of hybrid fiber laser-MIG welded Al-Mg alloy joints, *Applied Surface Science*, 298 (2014), 12–18
- ¹⁸ Z. Y. L. Cui, Z. Y. Wang, L. W. Ma, H. C. Du, C. W. Li, X. G. Wang, X., Effect of pH Value on the Electrochemical and Stress Corrosion Cracking Behavior of X70 Pipeline Steel in the Dilute Bicarbonate Solutions, *Journal of Materials Engineering and Performance*, 24 (2015)
- ¹⁹ S. Wang, J. Ding, H. Ming, Z. Zhang, J. Wang, Characterization of low alloy ferritic steel-Ni base alloy dissimilar metal weld interface by SPM techniques, SEM/EDS, TEM/EDS and SVET, *Materials Characterization*, 100 (2015), 50–60. doi:10.1016/j.matchar.2014.12.007
- ²⁰ F. Presuel-Moreno, H. Balasubramanian, Y. Y. Wu, Corrosion of Reinforced Concrete Pipes: An Accelerated Approach, in, 2013
- ²¹ X. Li, Y. Shao, W. Miao, Y. Liu, C. Liu, Galvanic corrosion behaviors of the low-carbon ferritic stainless steel ERW (electrical resistance welding) joint in the simulated seawater, *Anti-Corrosion Methods and Materials*, ahead-of-print (2020). doi:10.1108/ACMM-01-2020-2247
- ²² K. D. Ralston, N. Birbilis, C. H. J. Davies, Revealing the relationship between grain size and corrosion rate of metals, *Scripta Materialia*, 63 (2010), 1201–1204. doi:10.1016/j.scriptamat.2010.08.035
- ²³ K. D. Ralston, N. Birbilis, Effect of grain size on corrosion: A review, *Corrosion -Houston Tx-*, 66 (2010), 319–324. doi:10.5006/1.3462912
- ²⁴ D. Dwivedi, K. I. Lepková, T. Becker, Carbon steel corrosion: a review of key surface properties and characterization methods, *Rsc Advances*, 7 (2017), 4580–4610. doi:10.1039/C6RA25094G
- ²⁵ Y. Wang, A. Mukherjee, A. Castel, Non-destructive monitoring of incipient corrosion in reinforced concrete with top-bar defect using a combination of electrochemical and ultrasonic techniques, *Construction and Building Materials*, (2022)
- ²⁶ W. Chuaiphan, L. Srijaroenpramong, Effect of welding speed on microstructures, mechanical properties and corrosion behavior of GTA-welded AISI 201 stainless steel sheets, *Journal of Materials Processing Tech*, 214 (2014), 402–408. doi:10.1016/j.jmatprotec.2013.09.025
- ²⁷ Y. C. Lim, L. Squires, T. Y. Pan, M. Miles, G. L. Song, Y. Wang, Z. Feng, Study of mechanical joint strength of aluminum alloy 7075-T6 and dual phase steel 980 welded by friction bit joining and weld-bonding under corrosion medium, *Materials & Design*, 69 (2015), 37–43. doi:10.1016/j.matdes.2014.12.043
- ²⁸ L. Liu, R. Xu, Investigation of the corrosion behaviour of laser-TIG hybrid welded Mg alloys, *Corrosion Science*, 52 (2010), 3078–3085. doi:10.1016/j.corsci.2010.05.030
- ²⁹ J.G. Kim, Investigation of Weld Corrosion Effects on the Stress Behavior of a Welded Joint Pipe Using Numerical Simulations, *Metals and Materials International*, 25 (2019)
- ³⁰ B. L. Alwin, A. K. Vasudevan, M. Vasantharaja, Assessment of Stress Corrosion Cracking Resistance of Activated Tungsten Inert Gas-Welded Duplex Stainless Steel Joints, *Journal of Materials Engineering and Performance*, 26 (2017)
- ³¹ A. K. Lakshminarayanan, V. Balasubramanian, Assessment of sensitization resistance of AISI 409M grade ferritic stainless steel joints using Modified Strauss test, *Materials & Design*, 39 (2012), 175–185. doi:10.1016/j.matdes.2012.02.038
- ³² G. Choe, Y. Shinohara, G. Kim, S. Lee, J. Nam, Concrete Corrosion Cracking and Transverse Bar Strain Behavior in a Reinforced Con-

- crete Column under Simulated Marine Conditions, *Applied Sciences*, 10 (2020), 1794. doi:10.3390/app10051794
- ³³ H. M. Oleiwi, Y. Wang, M. Curioni, X. Chen, I. L. Shabalin, An experimental study of cathodic protection for chloride contaminated reinforced concrete, *Materials and Structures*, 51 (2018), 148. doi:10.1617/s11527-018-1273-1
- ³⁴ L. Zhao-Hui, L. Pei-Yuan, L. Wengui, L. Zhiyu, L. Yuelin, L. Peng, Empirical model of corrosion rate for steel reinforced concrete structures in chloride-laden environments, *Advances in Structural Engineering*, 22 (2018). doi:10.1177/1369433218783313
- ³⁵ J. Li, H. Li, Y. Liang, P. Liu, L. Yang, Y. Wang, Effects of heat input and cooling rate during welding on intergranular corrosion behavior of high nitrogen austenitic stainless steel welded joints, *Corrosion Science*, 166 (2020) 108441–108445. doi:10.1016/j.corsci.2020.108445
- ³⁶ K. Zhou, B. Wang, Y. Zhao, J. Liu, Corrosion and electrochemical behaviors of 7A09 Al-Zn-Mg-Cu alloy in chloride aqueous solution, *China Journal of Nonferrous Metals (English Edition)*. doi:10.1016/s1003-6326(15)63869-9
- ³⁷ Y. Savguira, T. H. North, S. J. Thorpe, Effect of grain size and residual stress on the corrosion resistance of friction stir spot welded AZ31B joints, *Materials & Corrosion*, (2016). doi:10.1002/maco.201608925
- ³⁸ J. Guo, S. Yang, C. Shang, Y. Wang, X. He, Influence of carbon content and microstructure on corrosion behaviour of low alloy steels in a Cl containing environment, *Corrosion Science*, 51 (2009), 242–251. doi:10.1016/j.corsci.2008.10.025
- ³⁹ H. W. Song, H. J. Kim, V. Saraswathy, T. H. Kim, A Micro-mechanics Based Corrosion Model for Predicting the Service Life of Reinforced Concrete Structures, *International Journal of Electrochemical Science*, 2 (2007) 341-354. doi:10.1002/fuce.200500252
- ⁴⁰ H. Li, R. Xu, Y. Song, Surface uniformity evaluation method of modified Ag/AgCl ocean electric field electrode based on SVET. *Chemical Physics Letters* (2023)
- ⁴¹ S.-C. Liu, Q. U. Wen-Juan. Scanning Micro Reference Electrode Testing of Localized Corrosion at Cu/Solderingtin Interface in Early Stage. *Corrosion & Protection* (2011)
- ⁴² Quevedo. The influence of vibration and probe movement on SVET measurements. *Corrosion Science: The Journal on Environmental Degradation of Materials and its Control* (2015)
- ⁴³ J. C. O'Shea, Innovative developments in scanning electrode techniques for corrosion monitoring and coating performance evaluation. Imperial College London (2000)
- ⁴⁴ I. Nakatsugawa, Y. Chino. Effect of Area Ratio on the Galvanic Corrosion of AZX611 Magnesium Alloy/A6N01 Aluminum Alloy Joint. *The Japan Institute of Metals and Materials* 12 (2021). doi:10.2320/MATERTRANS.MT-L2021011
- ⁴⁵ B. Losiewicz, M. Popczyk, M. Szklarska, A. Smolka, P. Osak, A. Budniok, Use of Scanning Vibrating Electrode Technique to Localized Corrosion Evaluation. *Diffusion and Defect Data. Solid State Data, Part B. Solid State Phenomena* 228b (2015), 353–368, doi:10.4028/www.scientific.net/SSP.228.353